Research Square

Preprints are preliminary reports that have not undergone peer review.
They should not be considered conclusive, used to inform clinical practice,
or referenced by the media as validated information.

Thermodynamic limits to secondary mineral formation from US enhanced weathering

Robert Rioux

rob.rioux@yale.edu

Yale University https://orcid.org/0000-0001-8841-5937

Ella Milliken

Yale University https://orcid.org/0009-0005-6996-3694

Christopher Reinhard

Georgia Institute of Technology https://orcid.org/0000-0002-2632-1027

Alicia Bateman

Virginia Polytechnic Institute and State University https://orcid.org/0009-0000-1835-7911

Sarah DeSanto

University of Pennsylvania

Sam Sidders

University of Pennsylvania

Declan Miller

Yale University

Boriana Kalderon-Asael

Yale University https://orcid.org/0000-0002-5442-8219

Dan Asael

Yale University https://orcid.org/0000-0002-4703-6081

Peter Raymond

Yale University https://orcid.org/0000-0002-8564-7860

James Saiers

Yale University https://orcid.org/0000-0002-0117-3347

Noah Planavsky

Yale University https://orcid.org/0000-0001-5849-8508

Physical Sciences - Article

Keywords:

Posted Date: November 17th, 2026

DOI: https://doi.org/10.21203/rs.3.rs-11731731/v1

License: This work is licensed under a Creative Commons Attribution 4.0 International License.
Read Full License

Additional Declarations: There is **NO** Competing Interest.

Thermodynamic limits to secondary mineral formation from US enhanced weathering

Robert A. Rioux[1,2], Ella Milliken[2,3], Christopher T. Reinhard[4], Alicia Bateman[5], Sarah B. DeSanto[6], Sam J. Sidders[6], Declan Miller[3], Boriana Kalderon-Asael[3], Dan Asael[3], Peter A. Raymond[1,2], James E. Saiers[1,2], Noah J. Planavsky[2,3]

[1] Yale School of the Environment, Yale University, New Haven, CT
[2] Yale Center for Natural Carbon Capture, Yale University, New Haven, CT
[3] Department of Earth and Planetary Sciences, Yale University, New Haven, CT
[4] School of Earth and Atmospheric Sciences, Georgia Institute of Technology, Atlanta, GA
[5] Department of Geosciences, Virginia Tech, Blacksburg, VA
[6] Department of Earth and Environmental Science, University of Pennsylvania, Philadelphia, PA

Abstract

It has become increasingly accepted that carbon dioxide removal (CDR) strategies will be necessary to prevent the worst impacts of climate change. As a result, CDR has been incorporated as a central component of climate policy frameworks and projections for climate impact in the coming century. Enhanced weathering (EW), the process of applying finely ground reactive rocks to croplands to accelerate chemical weathering and increase the conversion of atmospheric CO_2 to dissolved bicarbonate, has emerged as a promising, scalable, durable CDR approach with clear co-benefits for agricultural systems. However, there remain questions about the extent to which secondary mineral formation may constitute a significant carbon leakage pathway downstream of agricultural deployment. Here, we use an EW field trial and groundwater data from the coterminous US to develop a framework to gauge the likely risk of carbon leakage due to secondary mineral formation. We demonstrate that there are regions across the US with a low risk of carbon leakage through secondary mineral formation, and that these are typically the same regions where the process has the potential to provide the greatest economic and agricultural benefits to farmers. We suggest that this framework can be used to help derisk carbon accounting and crediting through EW in managed lands.

Main

Carbon dioxide removal (CDR) is increasingly recognized as necessary to meet climate targets, and enhanced weathering (EW) is being widely explored as a scalable CDR pathway that can simultaneously improve soil health and benefit farmers[1–3]. EW operates by applying ground, cation-rich rocks, such as basalt or limestone, to croplands that, when dissolved, release Ca and Mg and generate alkalinity that can be exported from landscapes, thereby removing CO_2 from the atmosphere. Global and regional assessments suggest that widespread EW deployment across croplands could support substantial CDR, with removals on the billion-ton scale[4–6]. This process could theoretically scale rapidly (e.g., on decadal timescales) by leveraging existing agricultural infrastructure and incentivizing farmer adoption through improved soil fertility and pH, as well as concurrent yield and economic gain[3,7,8]. These prospects have motivated significant public and private

investment in field trials and commercial activity[9–11]. However, the durability of this carbon removal ultimately depends on the fate of weathering products released in the field. If released cations are incorporated into newly formed clays, carbonates, or other secondary minerals, alkalinity generation and export will be reduced, and a portion of the initial carbon removal will be reversed. Secondary mineral formation is, therefore, an important source of uncertainty in EW accounting and modeling.

Whether secondary mineral precipitation meaningfully curbs EW-derived CDR will depend on the local geochemical and hydrologic conditions of the receiving environment, including the initial aqueous chemistry, mineral assemblage, drainage, and water residence time. Consequently, the susceptibility of an EW deployment to secondary mineral precipitation is likely to be strongly dependent on deployment location. Nevertheless, there is emerging concern that secondary-mineral formation may constitute a substantial and broadly applicable penalty on EW-derived CDR[12,13]. Despite the growing importance of this assumption for EW assessment and accounting, there is currently no framework grounded in field measurements of water chemistry for distinguishing environments where Ca- and Mg-bearing secondary phases may precipitate from those where their formation is thermodynamically unfavorable. Here, we propose using secondary mineral saturation states to provide such a framework.

Building on this framework, we explore whether secondary mineral formation represents a broadly applicable constraint on EW by quantifying measured mineral saturation states in shallow groundwater beneath a watershed-scale basalt deployment and across a continental groundwater dataset. We show that Ca- and Mg-bearing secondary phases remain largely thermodynamically inaccessible beneath both the basalt-amended agricultural field and across much of the shallow groundwater underlying major US agricultural regions. This is in marked contrast to natural basaltic catchments, which exhibit cation-bearing clay saturation levels that are often orders of magnitude greater than those observed in acidified agricultural lands that are likely to be targeted for EW amendments. These results demonstrate that susceptibility to secondary mineral formation—or reverse weathering—is strongly conditioned by the pre-existing geochemical state of the receiving soils and suggest that persistent secondary mineral precipitation is unlikely to represent a pervasive constraint for most US agricultural systems, which are already in need of greater soil pH management. More broadly, we propose mineral saturation states as a conservative, simple, field-based framework for identifying where secondary-mineral formation warrants concern and where it can be deprioritized in assessments of durable CDR through EW.

Application of a thermodynamic framework to an enhanced weathering field trial:

The thermodynamics of mineral precipitation are well established, and mineral saturation states can be readily estimated from aqueous geochemical measurements[14,15]. The Saturation index (*SI*) of a mineral is a fundamental parameter that compares the product of

the aqueous activities of dissolved mineral constituents (ion activity product; *IAP*) with their activities at thermodynamic equilibrium (solubility product; K_{sp}), such that:

$$SI = log_{10}\left(\frac{IAP}{K_{sp}}\right) \quad (1)$$

Mineral saturation indices quantify the thermodynamic potential for precipitation from observed water chemistry. Negative SI values indicate undersaturation, SI = 0 denotes equilibrium, and positive values indicate supersaturation. We use these relationships to establish a three-tier framework for screening secondary-mineral precipitation potential: low (SI < 0), moderate (0 ≤ SI ≤ 5), and high (SI > 5) potential. Although undersaturation prohibits net precipitation of the specified phase from the bulk solution at equilibrium, supersaturation indicates only that precipitation is thermodynamically favorable, not that it will occur. The distinction between moderate and high precipitation potential, therefore, provides a heuristic measure of the degree of supersaturation, recognizing that precipitation will also be subject to kinetic limitations despite being thermodynamically favorable.

Experimental lab studies demonstrate that secondary mineral precipitation can be kinetically inhibited even under strongly supersaturated conditions[16–20]. Supersaturation of several SI units has been observed without detectable aluminosilicate precipitation. In some Mg-silicate systems, homogeneous nucleation may require substantially greater supersaturation, with apparent thresholds approaching SI = 10–11[20]. Ca-silicates have been observed to exist at or above an SI of 5 in soil column experiments where basalt was added for the entire period of record with no observed precipitation of those Ca-silicates[21]. These observations support SI = 5 as an empirically informed, operational boundary rather than a universal kinetic threshold. Accordingly, we classify conditions with 0 ≤ SI ≤ 5 as having moderate precipitation potential, where mineral formation is thermodynamically favorable but kinetically uncertain, and SI > 5 as having high precipitation potential, indicating strong supersaturation and greater potential for mineral formation.

We apply this framework to shallow groundwater because its chemistry provides a hydrologically integrated measure of subsurface geochemical conditions, capturing the cumulative influence of water–rock interactions along flow paths that connect weathering environments to downstream waters. In contrast to localized soil-porewater measurements, groundwater chemistry integrates geochemical processes across contributing flow paths, while avoiding some of the mixing and dilution that occur after waters discharge into streams. These shallow subsurface pathways connect soil weathering processes to watershed-scale solute export, making groundwater a critical compartment for evaluating whether secondary mineral precipitation could limit the downstream transport of EW products.

We first apply this framework in a watershed-scale deployment of EW in a 5.15-km^2 mixed agricultural–forested catchment in a subtropical climate in the southern Virginia Piedmont near Clarksville, Virginia. The experimental site is a modified-tillage corn–wheat–soybean farm occupying ~15% of the catchment and is underlain by weathered Hapludult soils developed over alluvial-capped Precambrian granitic parent material. In June 2024, 1,270 metric tons of basalt (oxide composition, Table S1) were applied across 0.284 km^2 of cropland at an average rate of ~4.5 kg m^{-2}. Previous research suggests that substantial weathering of the basalt feedstock occurred, thereby releasing base cations into soil solutions [22,23]. To characterize subsurface geochemical characteristics of this deployment and the responses to basalt amendments, we monitored a network of shallow groundwater wells spanning contrasting hydrologic positions at the basalt-treated field and a nearby unamended comparison site with similar regional climate, lithology, and geologic setting. Wells were sampled repeatedly over two years (from July 2024 through June 2026) for major ions, alkalinity, trace elements, and *in situ* physicochemical parameters, providing spatially and temporally resolved groundwater observations to evaluate changes in geochemical conditions and mineral saturation states following basalt application.

Across the groundwater dataset, secondary mineral saturation states varied with mineral composition (Figure 1A; full table S2). Only kaolinite and gibbsite, non-cation-bearing aluminosilicates that do not reverse the carbon drawdown effects of weathering, were consistently at or above equilibrium, with median SIs of 1.15 and 1.21, respectively. In contrast, Ca- and Mg-bearing phases were predominantly undersaturated. Calcite and Ca-montmorillonite had median SIs of -4.70 and -4.27, respectively, and neither reached equilibrium in any sample, while Ca-beidellite was less undersaturated (median SI = -1.97). Undersaturation was substantially greater for Mg-bearing secondary minerals: median SIs were -30.99 for clinochlore-14A, -33.84 for sepiolite, and -23.69 for Mg-vermiculite, and all observations for these phases remained below SI = -10. Together, these patterns indicate that groundwater chemistry was relatively close to equilibrium with Al-rich weathering products but remained far from conditions that favor the precipitation of Ca-bearing, and especially Mg-bearing, secondary phases.

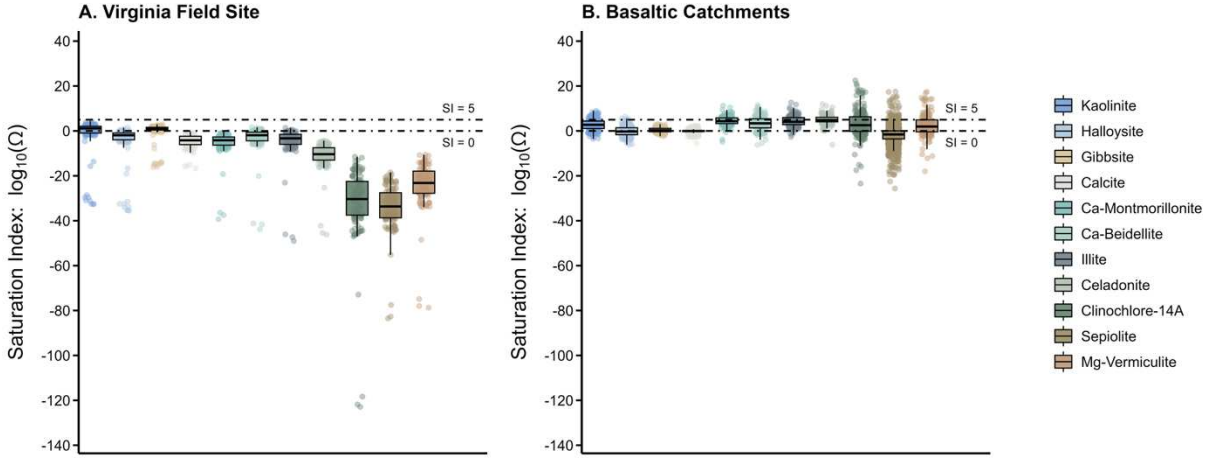


Figure 1: Saturation indices (SI) for selected clay minerals, carbonate, and secondary mineral phases calculated from shallow groundwater samples collected from (A) monitoring wells at the southern Virginia Piedmont field trial and (B) naturally basaltic catchments. Boxplots show medians and interquartile ranges, with points representing individual groundwater observations. Horizontal reference lines at SI = 0 and SI = 5 indicate the bounds from low-to-moderate and moderate-to-high precipitation risk, respectively. Positive SI values indicate supersaturation, whereas negative values indicate undersaturation.

These shallow groundwater conditions differ markedly from those reported in natural basaltic catchments, which were recently argued to be natural analogs for EW settings[13]. Across these natural basaltic groundwaters, Ca- and Mg-bearing minerals were substantially closer to equilibrium, producing a geochemical regime distinct from that observed beneath the basalt-amended agricultural field (Fig. 1B). For example, median saturation indices for Ca-montmorillonite and Ca-beidellite were oversaturated at 4.32 and 3.38, respectively, in basaltic groundwaters, compared with undersaturated values of −4.27 and −1.97 at our Virginia field site—an approximately four to eight orders of magnitude difference. For Mg-silicates, the differences were more extreme, with differences between basaltic catchments and our field sites differing by approximately fifteen orders of magnitude or more (e.g., clinochlore-14A (2.56 vs. −30.99), Mg-vermiculite (1.95 vs. −23.69), and celadonite (4.84 vs. −10.39)). This contrast illustrates a fundamental limitation of using natural basaltic Critical Zones as analogs for agricultural EW[13]: the thermodynamic behavior of degraded agricultural soils targeted for basalt application are likely to be very different from that of thick soil profiles developed through prolonged weathering of basaltic parent material. Instead, secondary-mineral thermodynamics following basalt application appear to remain strongly conditioned by the pre-existing Critical Zone environment. Consistent with this interpretation, saturation indices showed no significant temporal response to basalt application in linear mixed-effects models (Table S3).

Extrapolating reverse weathering risk across the conterminous United States

To evaluate geographic patterns in secondary-mineral saturation, we summarize estimated SIs across the coterminous US. The Southeastern US mirrors the deployment site in Virginia, with a similarly low risk of secondary mineral precipitation (Figure 2). Across shallow USGS groundwater wells (<15 m) in the southeastern US, median SIs for calcite, Ca-montmorillonite, and Ca-beidellite were −4.83, −1.22, and 0.80, respectively, compared with −4.70, −4.27, and −1.97 at the Virginia field site. Calcite was undersaturated in 96.6% of regional wells, whereas Ca-montmorillonite and Ca-beidellite were undersaturated in 65.3% and 41.3%, respectively. Other secondary silicates exhibited stronger undersaturation, including celadonite (median SI = −8.89) and Mg-vermiculite (−24.40). These findings extend our field study and suggest that the Southeastern US is thermodynamically well-suited for EW deployment, raising the question of whether similarly favorable conditions extend to other regions of the country.

Moving beyond the Southeastern US, pronounced regional differences in mineral saturation states emerged across the United States (Figure 2). Mg-bearing phases remained broadly undersaturated, while Ca-bearing clays were generally more saturated but still exhibited

low-to-moderate risk. Kaolinite and gibbsite were generally found to be moderate-risk, with localized high risk for kaolinite. The highest SIs were concentrated in the western Mountain and Pacific regions, particularly for Ca-bearing clays, although most observations remained within the moderate-risk range (Figure S1A). In contrast, the Northeastern, Eastern Mountain, and Southern regions exhibited the lowest SIs across the cation-bearing mineral assemblage. The Southern region was also the only region with a negative median SI for Ca-montmorillonite (−0.09). Notably, calcite remained undersaturated to near-equilibrium nationwide, with regional median SIs ranging from −3.48 to 0.27. This contrasts with the generally positive SIs of Ca-bearing clays, suggesting that those saturation states are strongly influenced by Al and Si activities rather than Ca. The agricultural Midwest, including the Great Lakes, Upper Midwest, and Heartland regions, exhibited generally higher SIs, although more than 90% of observations for both Ca-bearing clays remained within the low-to-moderate risk categories (Figure S1B). Regional median SIs are mapped by USDA NASS region in Figure S2. Collectively, these findings indicate that secondary clay mineral precipitation risk is highly spatially variable, with regions with clear risk and regions that are limited risk.

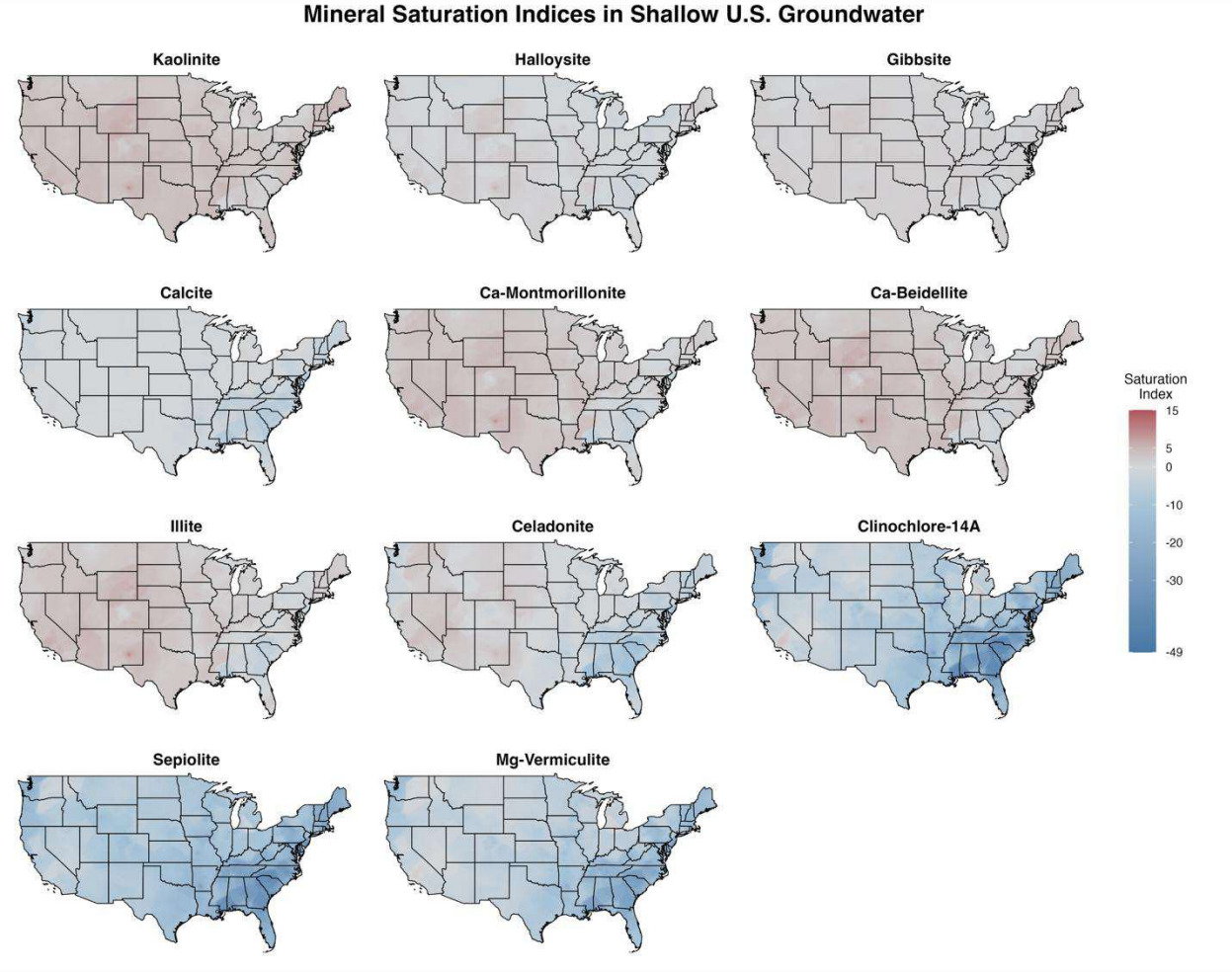


Figure 2: Mineral saturation indices for shallow groundwater across the coterminous United States. Well-level median saturation indices were spatially interpolated using k-nearest neighbors inverse-distance weighting (KNN-IDW; k = 8). All minerals are displayed on a common color scale, with blue indicating undersaturation (SI < 0), white indicating thermodynamic equilibrium (SI = 0), and red indicating supersaturation (SI > 0). Thermodynamic susceptibility to secondary-mineral precipitation is classified as low (SI ≤ 0), moderate (0 < SI ≤ 5), or high (SI > 5).

These findings are consistent with national-scale estimates of weathering potential based on climate and soil geochemistry. Across much of the western US, limited precipitation restricts soil-water flux and the export of weathering products, while prolonged leaching deficits favor alkaline soils and the accumulation of dissolved solutes. Together, these conditions can inhibit primary mineral dissolution and promote secondary mineral precipitation, limiting alkalinity export even where weathering occurs. In contrast, the wetter, more strongly weathered soils of the eastern US and portions of the Midwest generally exhibit lower pH and greater hydrologic transport, favoring continued mineral

dissolution and solute export. Agricultural tile drainage can further enhance this transport by connecting shallow soil water directly to streams[24,25]. These climatic, pedogenic, and hydrologic contrasts reinforce research demonstrating that EW potential depends not only on primary mineral dissolution rates but also on a given location's capacity to accommodate and export weathering products without substantial secondary mineral formation. Although conditions favorable for rapid basalt dissolution do not necessarily ensure efficient solute export, our results suggest that these properties can often coincide.

Agronomic acidity management aligns with favorable EW thermodynamics

The same base-cation depletion that contributes to low secondary-mineral saturation states also creates an agronomic need to replenish nutrients and manage soil acidity. This relationship is particularly relevant across the eastern and southeastern United States and portions of the Midwest, where extensive agricultural production on weathered soils often requires repeated liming to maintain crop productivity[26,27]. Raising soil pH in these systems can increase base saturation and nutrient availability while reducing Al and Mn toxicity, with meta-analyses demonstrating substantial crop yield benefits from alkaline amendments, particularly under strongly acidic conditions[28–30]. EW is likely to provide similar benefits by consuming acidity and releasing Ca, Mg, and other plant nutrients, allowing CDR to complement existing soil fertility management. Field trials and controlled experiments across maize, soybean, sorghum, oats, and rice have consistently reported crop yield increases of 9–37% following basalt amendment, often accompanied by improvements in soil pH and nutrient availability[31–34,8].

Intuitively, the landscapes with the lowest thermodynamic susceptibility to secondary mineral precipitation are also commonly those furthest from optimal agronomic conditions. A county-level comparison of median secondary-mineral SIs and agricultural soil-pH deficits (observed pH values relative to extension-recommended values) reveals substantial geographic overlap between these conditions, particularly across the Eastern US (Figure 3). Across much of the Southeast, Northeast, and Midwest, large agricultural soil-pH deficits coincide with groundwater conditions that are undersaturated with respect to Ca- and Mg-bearing secondary minerals. This coincidence strengthens the case for targeting agricultural landscapes for EW deployment foremost as a strategy for soil-acidity and base-cation management: basalt dissolution can consume acidity and supply Ca, Mg, and other nutrients where these inputs are already agronomically valuable, while the same base-depleted hydrogeochemical conditions leave comparatively large thermodynamic capacity to accommodate additional weathering products without promoting persistent secondary-mineral sequestration. In this framing, low secondary-mineral risk is not simply an advantage for CDR accounting; it is part of the same geochemical setting that creates the agronomic need for base cation amendment.

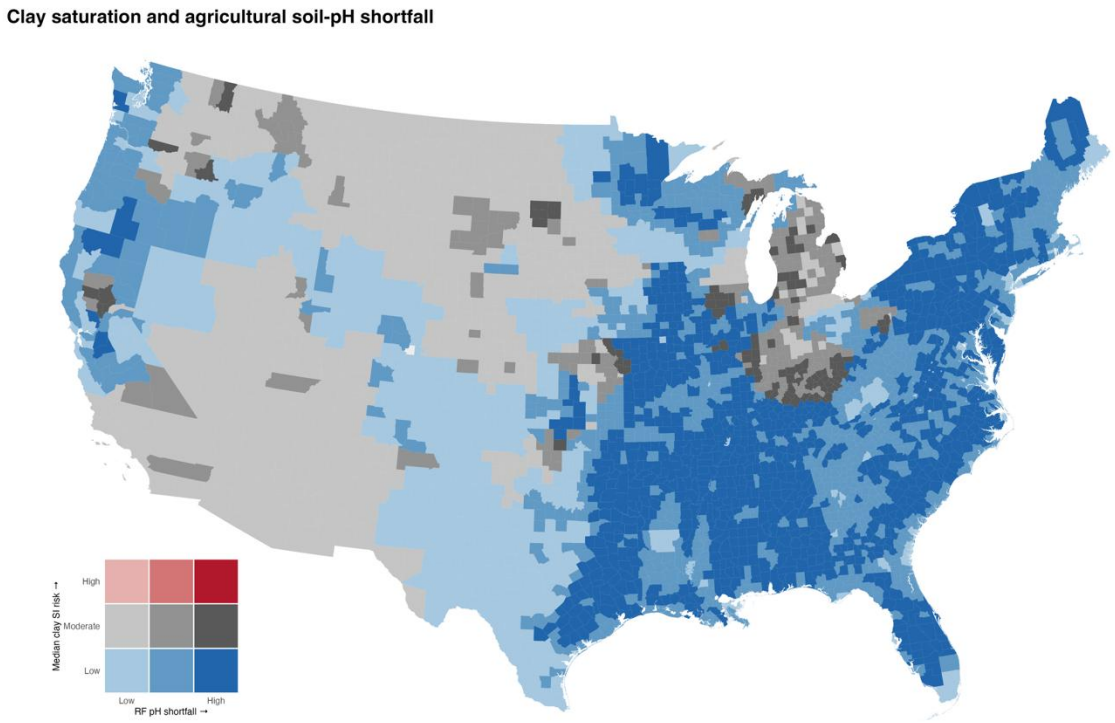


Figure 3: Geographic overlap of secondary-mineral saturation and agricultural soil-pH deficits at the county scale across the contiguous United States. County-level median saturation indices (SIs) for selected secondary minerals were classified as low (SI < 0), moderate (0 ≤ SI ≤ 5), or high (SI > 5). Agricultural soil pH deficits were derived from the random forest (RF) weighted scores reported by Woollen et al. (2026)[35] and divided into terciles. Dark blue indicates regions where low clay precipitation potential coincides with high agricultural soil-pH deficits.

To translate these regional patterns into an agriculturally relevant deployment context, we intersected 2025 crop distributions with the national saturation-state dataset and evaluated the median saturation state of seven cation-bearing secondary phases across cultivated land (Figure 4). The lowest median saturation states occur across much of the north- and south-eastern US, particularly in the lower Mississippi Valley, the Atlantic Coastal Plain, and portions of the Piedmont, whereas cultivated areas in parts of the northern Great Plains and western US generally occur closer to equilibrium (Figure 4a). Resolving these spatial patterns by the ten most extensively cultivated crop classes reveals substantial differences among major cropping systems (Figure 4b). Cotton shows the strongest association with low-risk saturation conditions, with 93.9% of its cultivated area occurring where the median SI across cation-bearing phases is below zero, followed by double-cropped winter wheat–soybean (88.1%) and rice (81.6%). Low-risk saturation conditions also predominate for sorghum (63.0%), soybean (58.7%), corn (56.8%), and oats (51.6%). In contrast, only 45.8% of winter wheat, 28.5% of barley, and 22.0% of spring wheat occur in the low-risk saturation class. None of the major crop classes contains any cultivated area classified as high precipitation risk on the basis of median SI (>5).

Mineral-specific saturation states reveal important differences in precipitation potential across cropping systems (Figure 4c). Mg-bearing phases, including clinochlore-14A, Mg-vermiculite, and sepiolite, remained strongly undersaturated across major crops, whereas Ca-montmorillonite, Ca-beidellite, and illite commonly exhibited positive median SIs of 2–4. Consequently, moderate precipitation potential largely reflects supersaturation with respect to a subset of clay minerals, rather than broadly favorable conditions for secondary-mineral precipitation. Smaller, geographically concentrated crop classes further highlight these regional differences (Figure 4d). Tobacco and sweet potatoes exhibited the lowest weighted median SIs (−4.90 and −4.81, respectively), followed by peanuts (−3.25). Sugarbeets, typically grown in the Upper Midwest and the Great Plains, and almonds, grown almost exclusively in California, are examples of regional crops that are near equilibrium but still undersaturated with respect to cation-bearing clays. Overall, these data suggest that much of the agricultural land across the United States is thermodynamically favorable for EW deployment, with generally low to moderate potential for secondary mineral precipitation and limited evidence of widespread conditions conducive to significant reverse weathering. This is consistent with the general view that calcium-bearing clays represent a negligible flux in the long-term global calcium and carbon cycles[36].

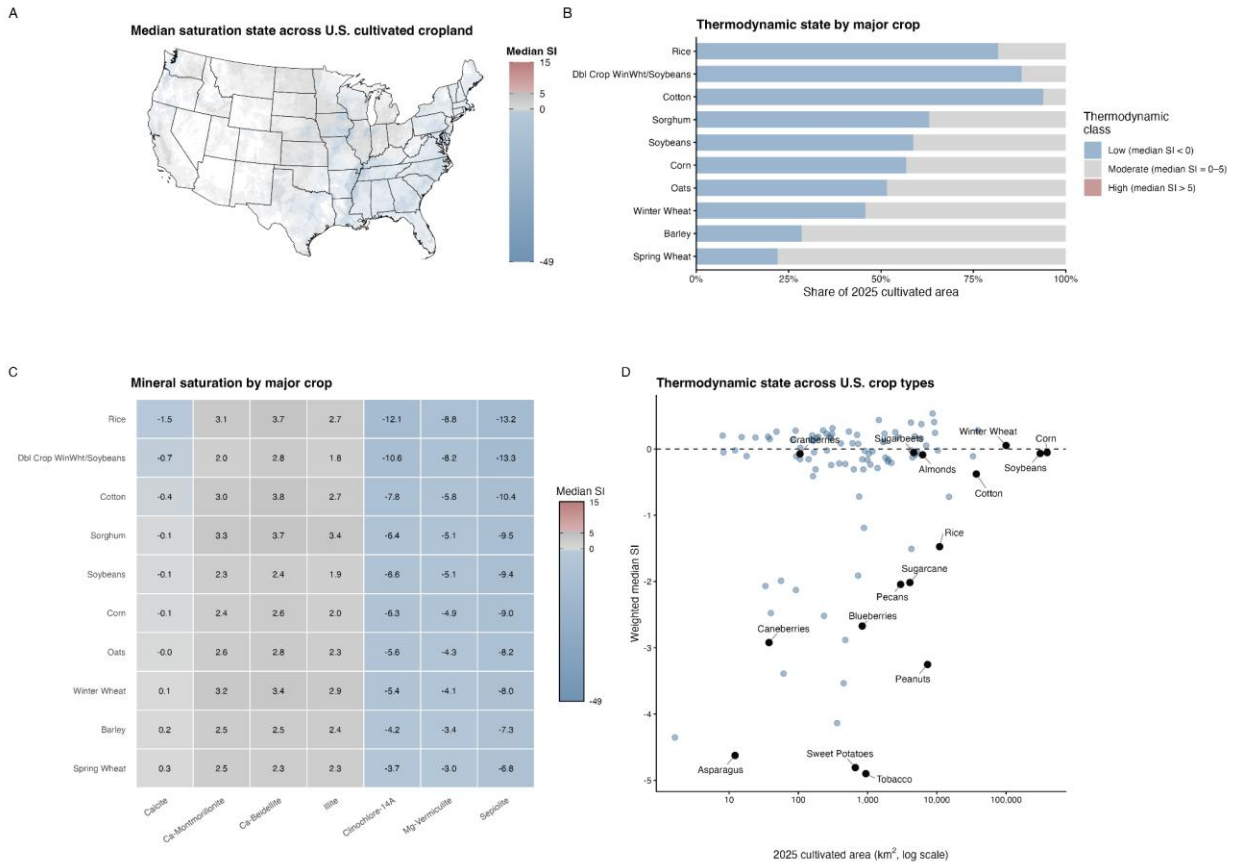


Figure 4: Thermodynamic saturation states across U.S. cultivated cropland and major crop systems. **a,** Median saturation index (SI) across seven cation-bearing secondary phases (calcite, Ca-montmorillonite, Ca-beidellite, illite, clinochlore-14A, Mg-vermiculite, and sepiolite) for grid cells containing cultivated cropland in

2025; negative values indicate undersaturation. **b,** Proportion of cultivated area for the ten largest U.S. crop classes occurring under low (median SI < 0), moderate (0 ≤ median SI ≤ 5), and high (median SI > 5) thermodynamic precipitation potential. **c,** Area-weighted median SI for each of the seven cation-bearing phases across the same major crop classes, showing that moderate crop-level saturation states are driven primarily by Ca-bearing clays, whereas Mg-bearing phases remain strongly undersaturated. **d,** Relationship between national cultivated area and area-weighted median SI across all cultivated crop classes. Labeled crops highlight major or geographically concentrated systems spanning conditions from strongly undersaturated to near-equilibrium. Crop distributions are based on 2025 USDA Cropland Data Layer classifications and therefore represent the hydrogeochemical conditions associated with where crops were cultivated in that year rather than intrinsic crop-specific properties.

Implications for EW deployment and assessment

Distinguishing between reverse weathering and other temporal lags in alkalinity throughput is particularly important, as secondary mineral formation is increasingly invoked as a potentially substantial loss pathway for EW-derived CDR. Secondary clays and carbonates can clearly form during silicate weathering, but thermodynamic potential alone does not establish that they will form in a particular deployment, nor that they will sequester a quantitatively important fraction of EW-derived cations. Their formation first requires that the receiving solution approach saturation with respect to the relevant phase, a condition that depends strongly on pre-existing aqueous chemistry, mineralogy, hydrology, and weathering history. Consequently, secondary-mineral losses cannot simply be assigned from feedstock composition, laboratory observations, modeled reaction networks, or attenuation observed in natural weathering systems without establishing that comparable thermodynamic conditions occur at the deployment site. Recent assessments that emphasize potentially large alkalinity losses through secondary mineral formation and downstream reactions therefore identify important pathways, but their magnitude remains poorly constrained in agricultural EW systems[12,13]. Conversely, modeled basalt dissolution alone does not guarantee complete downstream export, reinforcing the need to constrain these processes directly from the receiving environment. Available field evidence suggests that such constraints can substantially change expectations for solute retention. Recent research has reconstructed more than a century of agricultural liming across the Mississippi River Basin and estimated that approximately 90% of the ideal CO_2-removal potential of applied lime was ultimately expressed as increased riverine bicarbonate export, with major lags driven primarily by acid-base chemical dynamics rather than by secondary mineral precipitation[37].

More broadly, the results from our framework highlight the need to ground proposed EW loss pathways in field observations of the environments where deployment actually occurs. Laboratory experiments and reactive transport models are essential for identifying possible outcomes from large-scale EW deployments, but field trials are needed to determine whether the chemical conditions required for those outcomes are ever reached, how long they persist, and whether they materially affect alkalinity export. Our SI framework and analysis provide a particularly useful first step because they are straightforward, directly constrained by measured water chemistry, and rest on a basic thermodynamic requirement: a mineral cannot precipitate from a solution that is undersaturated with

respect to that phase. This approach can be easily integrated into carbon accounting protocols as an initial screening tool for understanding local deployment risk, or for applying any necessary discounts to deployments post-application. Further, this framework provides clear, rigorous, and conservative values that operators could maintain as benchmarks for local reapplication to prevent reverse weathering-driven losses.

Methods

Site Description and Experiment

Our field site is located within a 5.15 km^2 agricultural and forested catchment (37.91% and 42.32%, respectively) in Clarksville, VA, in the Piedmont region of southern Virginia (Figure 4). The average temperature at our field site is 15.7 ºC, with the warmest temperatures typically recorded in July (the maximum from 1991 to 2020 was 33.2 ºC) and the coldest in January (the minimum from 1991 to 2020 was -1.8 ºC). The average annual precipitation is approximately 1105 mm, with July typically being the wettest month, at around 125 mm. Our field site is situated on a no-till corn-wheat-soybean agricultural farm, which accounts for approximately 15% of the total watershed. The soil across the study region is a fine, mixed, subactive, thermic, oxyaquatic hapludult, with a parent material of alluvial-capped Precambrian granite with outcroppings of foliated biotite quartz and other silicate rocks. For the first year of the study (2024), winter wheat was harvested in early June, and soybeans were planted in late June. Soybeans were harvested in October 2024, and a mixed rye cover crop was applied before being terminated in early March. Corn was planted in April 2025. Further information on soil composition and chemistry can be found in Milliken et al. 2025. In June 2024, 1400 tons of basalt were spread across 28.4 ha at an average rate of approximately 50 tons/ha (blue areas in Figure 6). The basalt feedstock was sourced from Sunrock Industries in Butner, NC, and its oxide weight composition is shown in Table S1.

Instrumentation and Groundwater Wells

From May to June 2024 (before the basalt application), we installed twelve shallow groundwater monitoring wells at the primary (basalt-amended) field site, distributed across hydrologically distinct landscape positions to capture spatial variability in subsurface flowpaths and geochemical conditions (Figure S3A). Wells were drilled to bedrock or to a maximum depth of approximately 6 m below ground surface, with an average screened depth of ~4 m. A secondary field site that did not receive basalt amendment was instrumented to provide a quasi-control for comparison (Figure S3B). While this site differs in soil properties, land management practices, and baseline groundwater chemistry, it shares similar climate, lithology, and regional geologic setting with the primary site. The secondary site features a comparable network of eleven shallow groundwater wells (mean depth ~3.5 m), two deeper wells (7–9 m), and several shallow installations (~1.2 m), with most wells located in riparian positions along the stream corridor.

Sample Collection and Analysis

These wells were sampled approximately quarterly from July 2024 to March 2025 and bimonthly from June 2025 to January 2026, covering multiple seasons following basalt application in June 2024. Wells were measured on site for pH, specific conductance, and

temperature with a YSI ProQuatro handheld multiprobe equipped with a continuously pumped flow-through cell. Water samples were collected after pH and specific conductance readings stabilized, filtered through 0.22 µm PES filters on-site, and stored in acid-washed, groundwater-rinsed high-density polyethylene (HDPE) bottles. The samples for trace metal analysis were acidified by adding concentrated, ultrapure nitric acid to a pH < 2 in the lab and within 48 hours of collection. All the samples were transported on ice back to the lab and stored at 4 °C until analysis. Major cations (Ca^{2+}, Mg^{2+}, Na^{+}, K^{+}) and major anions (Cl^{-}, NO_3^{-}, SO_4^{2-}) were measured via ion chromatography (Metrohm, USA) using Metrosep C4-150/4.0 and Metrosep A Supp 5-150/4 columns, respectively. Alkalinity was measured using a Gran Titration method on an alkalinity titrator (Mettler Toledo, USA). The major ion and alkalinity measurements were performed at Yale Analytical and Stable Isotope Center (YASIC), while the trace metal concentrations were measured in the Yale Geochemistry Center, in the Department of Earth and Planetary Sciences.

Together, these datasets provide spatially distributed groundwater observations suitable for evaluating the influence of basalt amendment on subsurface geochemical conditions and mineral saturation states at the watershed scale, as both sites were sampled under a comparable temporal framework and analyzed for the same suite of chemical constituents, with only minor variation in sampling coverage among individual wells.

Basaltic Catchment Data

To place groundwater chemistry observed at the EW field site in a broader geochemical context, we assembled reference water chemistry datasets from natural basaltic aquifers. These included groundwater from Kīlauea Volcano, Hawai‘i[38,39]; northern Iceland[40]; the Columbia River Basalt Group in Washington[41]; and the eastern Snake River Plain aquifer in Idaho[42]. All records were standardized to a common set of chemical variables before geochemical calculations. The Kīlauea datasets included groundwater from the deep NSF (Keller) well within the summit hydrothermal system and from the Lower East Rift Zone, whereas the northern Iceland dataset included surface water and groundwater from tholeiitic basalt terrain, with only groundwater observations retained. Columbia River Basalt Group records were obtained from the accompanying Washington Geological Survey groundwater chemistry database and restricted to observations associated with the basalt aquifer system. The eastern Snake River Plain dataset consisted of groundwater chemistry from 36 wells sampled in June 2017.

USGS Groundwater Data

Groundwater chemistry data for the conterminous United States were retrieved in R (v.4.5.0) using the `dataRetrieval` package and the USGS Water Data for the Nation Samples API. Records collected from 1 January 2010 through the date of data retrieval in September 2026 were queried separately by state using read_waterdata_samples, with siteTypeName = "Well" and the basicphyschem data profile. Target constituents were alkalinity (USGS parameter codes 00418, 00421, 29801, 29802, 29803, 39036, 39086, 39087, 99431, 00410 and 90410), pH (00400, 00403 and 00408), Ca (00915 and 91051), Mg (00925 and 91052), Na (00930 and 91053), K (00935 and 91054), Al (01106 and 04096), dissolved silica (00955) and

water temperature (00010). Temperature was retained when available, but was not required for inclusion. Calcium, Mg, Na, K, Al, and silica results were restricted to measurements identified by USGS as filtered or dissolved water samples.

Individual USGS sampling activities were retained as the fundamental observational unit so that measurements collected from the same well on different dates remained independent records. Site identifiers, sampling-activity identifiers, collection date and time, geographic coordinates, and available well metadata were preserved throughout processing. Results reported below analytical detection limits were retained rather than discarded. For observations explicitly designated as "Not Detected", the reported censoring level was identified from the associated detection-limit fields, and a concentration equal to one-half of that level was used; observations lacking both a measured concentration and a usable numerical censoring limit were excluded. Concentrations reported in $\mu g\ l^{-1}$ were converted to $mg\ l^{-1}$ where necessary.

Replicate results representing the same sampling activity, analyte, parameter code, and reporting unit were averaged before the dataset was reshaped to one record per sampling activity. Where multiple pH parameter codes occurred within a sampling activity, field pH (00400) was preferentially retained over laboratory pH (00403), followed by parameter code 00408. Other activity–analyte combinations with unresolved differences in parameter codes or reporting units were excluded rather than arbitrarily combined. A complete chemistry subset was then defined as a set of sampling activities that included alkalinity, pH, Ca, Mg, Na, K, Al, and silica. Monitoring-location metadata were retrieved separately and joined to the chemistry records by USGS site identifier.

Because the comparison was intended to characterize shallow groundwater most relevant to near-surface critical-zone weathering, the national dataset was further restricted using USGS well-construction metadata. Only wells with a reported positive constructed depth of ≤50 ft were retained; wells lacking a usable construction depth were excluded from the shallow-groundwater subset.

For each published or archived dataset, the original sample identifier, site or well identifier where available, sampling date, water type, temperature, pH, and reported major-element chemistry were retained. The primary variables extracted were Ca, Mg, Na, K, Al, silica, alkalinity, Cl, SO_4, and NO_3, although not every constituent was available for every source. Concentrations were converted to common units and chemical reporting bases before datasets were combined. Molar concentrations were converted to mass concentrations using constituent-specific molecular weights, $\mu g\ l^{-1}$ values were converted to $mg\ l^{-1}$, and silica and alkalinity measurements reported on different chemical bases were converted to the common basis used for subsequent geochemical calculations. Values reported as below a numerical detection or reporting limit were assigned one-half of the stated limit, consistent with the treatment of censored USGS observations. Constituents that were not measured or for which no numerical reporting limit was available were retained as missing and were not otherwise imputed.

USDA 2025 Cropland Data and pH Deficiency

To evaluate the relationship between mineral saturation and agricultural land use, we obtained the 2025 USDA NASS Cropland Data Layer (CDL), resampled to 30-m spatial resolution[43]. We intersected the CDL with the interpolated national SI dataset, represented by a 0.15° geographic grid, to quantify cultivated area associated with each estimated saturation state. Grid cells were converted to polygons and projected into the CDL coordinate reference system before extracting crop classifications using the *terra* R package. The number of 30-m raster cells assigned to each crop was multiplied by the corresponding cell area (900 m^2) to calculate the cultivated area by crop type within each SI grid cell. We excluded nonagricultural land-cover classes, pasture, hay, alfalfa, fallow cropland, and aquaculture to focus the analysis on cultivated fields and specialty crops. Crop-specific saturation states were summarized using area-weighted medians and interquartile ranges, with cultivated area serving as the weighting variable.

To evaluate precipitation potential across cultivated land, we calculated a composite SI as the median saturation index of seven cation-bearing secondary phases: calcite, Ca-montmorillonite, Ca-beidellite, illite, clinochlore-14A, Mg-vermiculite, and sepiolite. Composite values were classified into low, moderate, and high precipitation-potential categories using the thresholds defined above. For the ten most extensive crop classes, we calculated the proportion of cultivated area within each category and determined mineral-specific area-weighted median SIs. We additionally evaluated all retained crop classes to examine relationships between the national cultivated area and the composite saturation state.

Finally, we compared groundwater saturation states with agricultural soil pH deficiency using county-level estimates from Woollen et al. (2026)[35]. Their study combined random-forest predictions of soil pH with crop-specific agronomic pH recommendations to quantify the extent and severity of soil acidity across the contiguous United States. We used their cumulative pH undershooting metric, which weights the number of cropland raster cells below the recommended pH by the magnitude of their pH shortfall. To establish spatial correspondence with our groundwater dataset, we intersected the 0.15° SI grid with county boundaries and calculated an area-weighted median composite SI for each county using the geographic overlap between grid cells and county polygons. These county-level saturation estimates were then paired with the soil pH undershooting values to construct a bivariate map identifying agricultural regions where low secondary-mineral saturation coincides with substantial agronomic soil acidity.

PHREEQC Saturation Index Calculations

Geochemical modeling was conducted using PHREEQC v3.8.6[15] with a custom thermodynamic database, based on the Lawrence Livermore National Laboratory database, supplemented with halloysite from Minteq (v4) and Mg-Vermiculite from Thermoddem (v1.10). A total of 185 groundwater samples were analyzed, each characterized by measured pH, temperature, and major ion chemistry (Ca^{2+}, Mg^{2+}, Na^{+}, K^{+}, Cl^{-}, SO_4^{2-}, and

HCO_3^-), supplemented by trace element data (Al and Si). Titrated total alkalinity values (μmol kg^{-1}) were converted to HCO_3^- (mg L^{-1}) assuming bicarbonate dominance. Input files were programmatically generated in R to define individual Solution blocks for each sample, each equilibrated with a representative mineral phase (Kaolinite, Halloysite, Gibbsite, Calcite, Ca-Montmorillonite, Illite, Clinochlore-14A, Sepiolite, Celadonite, Ca-Beidellite, and Mg-Vermiculite). PHREEQC simulations were run in batch mode, and the resulting SIs were extracted from the model output in R to assess clay stability and saturation trends across groundwater wells.

Linear Mixed Effects Modeling

We used linear mixed-effects (LME) regression to evaluate how clay mineral SIs varied with time, hydrologic position, and basalt treatment across the two experimental fields. Separate models were fit for each clay phase (kaolinite, calcite, and illite, etc.). Each model included *Time*, *Location*, and *Treatment* as fixed effects, along with all two- and three-way interactions. *Time* was represented as a continuous variable denoting months since basalt application; *Location* distinguished upland and riparian wells (with upland as the reference category); and *Treatment* indicated whether samples were collected from the basalt-amended or quasi-control field. A random intercept was included for each well to account for repeated measurements and baseline differences among wells.

This framework evaluates whether temporal or spatial trends in clay mineral saturation differ between the basalt-treated and reference sites, and whether riparian wells exhibit distinct temporal trajectories compared to upland wells. The LME regression is expressed as:

$$\begin{aligned} SI_{ijk} = \mu + \beta_1 Time_j + \beta_2 Location_i + \beta_3 Treatment_k \\ + \beta_4(Time_j \times Location_i) + \beta_5(Time_j \times Treatment_k) \\ + \beta_6(Location_i \times Treatment_k) \\ + \beta_7(Time_j \times Location_i \times Treatment_k) + u_i + \varepsilon_{ijk} \end{aligned} \quad (2)$$

where SI_{ijk} is the saturation index for a given clay in well *i* at time *j* within treatment *k*; μ is the expected value of SI at the reference location and treatment; β terms represent fixed effects of time, position, and treatment; u_i is a random intercept for each well; and $\varepsilon_{(ijk)}$ is the residual error.

All statistical analyses were conducted in R (v4.5.0) using the lme4 (v1.1-37)[44] and lmerTest (v3.1-3)[45] packages. Models were fit using the lmer function, and outputs included fixed- and random-effect estimates, Wald *t*-statistics, and approximate *p*-values based on Satterthwaite degrees of freedom. Type III ANOVA tables were also used to evaluate the relative importance of main effects and interactions. Model residuals were examined to verify assumptions of normality and homoscedasticity, and no transformation of SI values was required. Fixed-effect estimates and associated tests were used to determine whether

clay minerals exhibited significant temporal or spatial trends, and whether these patterns differed between the basalt-amended and reference fields.

Works Cited:

1. IPCC. *AR6 Synthesis Report*. https://www.ipcc.ch/report/sixth-assessment-report-cycle/ (2023).
2. Hartmann, J. *et al.* Enhanced chemical weathering as a geoengineering strategy to reduce atmospheric carbon dioxide, supply nutrients, and mitigate ocean acidification. *Rev. Geophys.* **51**, 113–149 (2013).
3. Swoboda, P., Döring, T. F. & Hamer, M. Remineralizing soils? The agricultural usage of silicate rock powders: A review. *Sci. Total Environ.* **807**, 150976 (2022).
4. Strefler, J., Amann, T., Bauer, N., Kriegler, E. & Hartmann, J. Potential and costs of carbon dioxide removal by enhanced weathering of rocks. *Environ. Res. Lett.* **13**, 034010 (2018).
5. Beerling, D. J. *et al.* Potential for large-scale CO2 removal via enhanced rock weathering with croplands. *Nature* **583**, 242–248 (2020).
6. Beerling, D. J. *et al.* Transforming US agriculture for carbon removal with enhanced weathering. *Nature* **638**, 425–434 (2025).
7. Renforth, P. The potential of enhanced weathering in the UK. *Int. J. Greenh. Gas Control* **10**, 229–243 (2012).
8. Milliken, E. *et al.* Significant yield benefits from basalt soil amendments in the Southeastern US. *CDRXIV* https://cdrxiv.org/preprint/413 (2026).
9. US Department of Energy. Project Selections for FOA 3082: Carbon Negative Shot Pilots. *Energy.gov* https://www.energy.gov/hgeo/project-selections-foa-3082-carbon-negative-shot-pilots (2024).

10. Frontier. Lithos Project Page. *Frontier* https://frontierclimate.com/portfolio/lithos (2023).
11. Frontier. Frontier buyers sign $33M in offtake agreements with Eion. *Frontier* https://frontierclimate.com/writing/eion (2025).
12. Isson, T. & West, A. J. Can enhanced alkalinity store carbon durably? *Science* **392**, 808–810 (2026).
13. Derry, L. A., Maher, K. & Chadwick, O. A. Critical zone processes limit alkalinity export from natural basaltic systems. *Nature* 1–6 (2026) doi:10.1038/s41586-026-10936-3.
14. Drever, J. I. *The Geochemistry of Natural Waters: Surface and Groundwater Environments*. (Prentice-Hall, 1997).
15. Parkhurst, D. L. & Appelo, C. A. J. *Description of Input and Examples for PHREEQC Version 3—A Computer Program for Speciation, Batch-Reaction, One-Dimensional Transport, and Inverse Geochemical Calculations*. (2013) doi:http://pubs.usgs.gov/tm/06/a43/.
16. May, H. M., Kinniburgh, D. G., Helmke, P. A. & Jackson, M. L. Aqueous dissolution, solubilities and thermodynamic stabilities of common aluminosilicate clay minerals: Kaolinite and smectites. *Geochim. Cosmochim. Acta* **50**, 1667–1677 (1986).
17. Vybíhal, K. & Faimon, J. INTERAKCE BAYERITU A KYSELINY KŘEMIČITÉ V SLABĚ KYSELÉM PROSTŘEDÍ ZA NORMÁLNÍCH PODMÍNEK. *Geol. Res. Morav. Sil.* **12**, (2005).
18. Iniesto, M. *et al.* Preservation in microbial mats: mineralization by a talc-like phase of a fish embedded in a microbial sarcophagus. *Front. Earth Sci.* **3**, (2015).

19. Baldermann, A., Mavromatis, V., Frick, P. M. & Dietzel, M. Effect of aqueous Si/Mg ratio and pH on the nucleation and growth of sepiolite at 25 °C. *Geochim. Cosmochim. Acta* **227**, 211–226 (2018).
20. Arizaleta, M. L., Nightingale, M. & Tutolo, B. M. A rate law for sepiolite growth at ambient temperatures and its implications for early lacustrine diagenesis. *Geochim. Cosmochim. Acta* **288**, 301–315 (2020).
21. Iff, N., Renforth, P. & Pogge von Strandmann, P. A. E. The dissolution of olivine added to soil at 32°C: the fate of weathering products and its implications for enhanced weathering at different temperatures. *Front. Clim.* **6**, (2024).
22. Milliken, E., Woodley, A. & Planavsky, N. J. Direct Measurement of Carbon Dioxide Removal Due to Enhanced Weathering. *Environ. Sci. Technol. Lett.* **12**, 970–976 (2025).
23. Milliken, E. *et al.* Evidence of rapid basalt dissolution in Southeastern US croplands. *CDRXIV* https://cdrxiv.org/preprint/551 (2026).
24. Schilling, K. E. & Helmers, M. Effects of subsurface drainage tiles on streamflow in Iowa agricultural watersheds: Exploratory hydrograph analysis. *Hydrol. Process.* **22**, 4497–4506 (2008).
25. Podzorski, H. L. & Ryberg, K. R. *A Framework for Understanding the Effects of Subsurface Agricultural Drainage on Downstream Flows*. *Scientific Investigations Report* https://pubs.usgs.gov/publication/sir20255023 (2025) doi:10.3133/sir20255023.

26. Enesi, R. O. *et al.* Liming remediates soil acidity and improves crop yield and profitability - a meta-analysis. *Front. Agron.* **5**, (2023).
27. Tsao, S. S.-E. *et al.* A spatially explicit dataset of agriculture liming across the contiguous United States. *Earth Syst. Sci. Data Discuss.* 1–32 (2025) doi:10.5194/essd-2025-411.
28. Zhang, S. *et al.* Effects of soil amendments on soil acidity and crop yields in acidic soils: A world-wide meta-analysis. *J. Environ. Manage.* **345**, 118531 (2023).
29. Enesi, R. O. *et al.* Liming remediates soil acidity and improves crop yield and profitability - a meta-analysis. *Front. Agron.* **5**, (2023).
30. Wenyika, P., Enesi, R. O., Gorim, L. Y. & Dyck, M. Effects of liming on soil physical and chemical properties in Europe and North America: A review. *Agrosystems Geosci. Environ.* **8**, e70175 (2025).
31. Kelland, M. E. *et al.* Increased yield and CO2 sequestration potential with the C4 cereal Sorghum bicolor cultivated in basaltic rock dust-amended agricultural soil. *Glob. Change Biol.* **26**, 3658–3676 (2020).
32. Beerling, D. J. *et al.* Enhanced weathering in the US Corn Belt delivers carbon removal with agronomic benefits. *Proc. Natl. Acad. Sci.* **121**, e2319436121 (2024).
33. Skov, K. *et al.* Initial agronomic benefits of enhanced weathering using basalt: A study of spring oat in a temperate climate. *PLOS ONE* **19**, e0295031 (2024).
34. Jordan, J. S. *et al.* Enhanced rock weathering for improved smallholder farmer welfare: An at-scale case study for rice agriculture in India. *CDRXIV* https://cdrxiv.org/preprint/483 (2026).

35. Woollen, B. J. *et al.* Significant Scope for Improvement of Soil Acidity Management in US Croplands. *CDRXIV* https://cdrxiv.org/preprint/535 (2026).
36. Berner, E. K. & Berner, R. A. *Global Environment: Water, Air, and Geochemical Cycles*. (Prentice Hall, 1996).
37. Suhrhoff, T. J. *et al.* Agricultural liming is a carbon sink in the Mississippi River Basin. *Nature* **658**, 113–118 (2026).
38. Hurwitz, S. *et al.* Mixing of magmatic volatiles with groundwater and interaction with basalt on the summit of Kilauea Volcano, Hawaii. *J. Geophys. Res. Solid Earth* **108**, (2003).
39. McCleskey, R. B. *et al.* Groundwater chemistry in the Lower East Rift Zone and summit of Kilauea Volcano, Hawai'i. U.S. Geological Survey https://doi.org/10.5066/P9BVN915 (2020).
40. Arnórsson, S., Gunnarsson, I., Stefánsson, A., Andrésdóttir, A. & Sveinbjörnsdóttir, Á. E. Major element chemistry of surface- and ground waters in basaltic terrain, N-Iceland.: I. primary mineral saturation. *Geochim. Cosmochim. Acta* **66**, 4015–4046 (2002).
41. Svadlenak, E. E. & Florea, L. J. *Groundwater Chemistry in the Columbia River Basalt Group, Columbia Basin, Washington*. 21 p https://washingtonstategeology.wordpress.com/2025/08/21/new-columbia-basin-groundwater-chemistry-database-and-analysis-published/ (2025) doi:https://dnr.wa.gov/sites/default/files/2025-07/ger_ri48_groundwater_columbia_basin.zip.

42. Skinner, K. D. *Groundwater-Quality Data from the Eastern Snake River Plain Aquifer, Jerome and Gooding Counties, South-Central Idaho, 2017*. *Data Series* https://pubs.usgs.gov/publication/ds1085 (2018) doi:10.3133/ds1085.
43. USDA, N. CroplandCROS. (2025).
44. Bates, D., Mächler, M., Bolker, B. & Walker, S. Fitting Linear Mixed-Effects Models Using lme4. *J. Stat. Softw.* **67**, 1–48 (2015).
45. Kuznetsova, A., Brockhoff, P. B. & Christensen, R. H. B. lmerTest Package: Tests in Linear Mixed Effects Models. *J. Stat. Softw.* **82**, 1–26 (2017).

Acknowledgements
We thank the Yale Analytical and Stable Isotope Center (YASIC) and Yale Geochemistry Center for their help in the measurements of water samples. We also acknowledge the graciousness of A. Wilbourne, who allowed us to conduct our experiment on his land.

Funding
The authors acknowledge funding from Microsoft for the deployment of this EW project. NJP acknowledges funding from Microsoft, Fund for Science and Technology, and EDF.

Author contributions
R.A.R., E.M., J.E.S., and N.J.P. conceived, designed, and established the experiment. C.T.R., J.E.S., P.A.R., and N.J.P. supervised the project. R.A.R. led the field sampling, conducted the water chemistry analysis with A.B., S.B.D., S.J.S., and D.M., and performed data analysis and modeling. B.K.-A. and D.A. supervised the water chemistry analyses. C.T.R. and N.J.P. provided the conceptual framework. R.A.R. drafted the paper, and E.M., C.T.R., A.B., S.B.D., S.J.S., D.M., B.K.-A., D.A., P.A.R., J.E.S., and N.J.P. contributed to editing and revision. All authors approved the final version.

Competing Interest Statement
NJP and CTR were co-founders of Lithos Carbon but have no remaining ties to the company. The remaining authors declare that they have no competing interests.

Correspondence and requests for materials should be addressed to Robert A. Rioux

Data Availability
The data that support the findings of this study are available from the corresponding author upon reasonable request.

Supplementary Files

This is a list of supplementary files associated with this preprint. Click to download.

- SIThermodynamicLimitsFinal.docx